1 **Title:** Super-resolution microscopy of the ß-carboxysome reveals a homogenous matrix

2

3

4 **Authors:** Matthew J. Niederhuber *,[†], Talley J. Lambert[‡], Clarence Yapp[§], Pamela A.

5 Silver*,[†], Jessica K. Polka*,[†]

6

7 **Affiliations:**

8 * Department of Systems Biology, Harvard Medical School, 02115, Boston,

9 Massachusetts, United States.

10 † Wyss Institute for Biologically Inspired Engineering, Harvard University, 02115,

11 Boston, Massachusetts, United States.

12 ‡. Department of Cell Biology, Harvard Medical School, 02115, Boston, Massachusetts,

13 United States.

14 §. Image and Data Analysis Core, Harvard Medical School, 02115, Boston,

15 Massachusetts, United States.

16

17 **Abstract:**

18   Carbon fixation in cyanobacteria makes a major contribution to the global carbon

19 cycle. The cyanobacterial carboxysome is a proteinaceous microcompartment that

20 protects and concentrates the carbon-fixing enzyme RuBisCO in a paracrystalline lattice,

21 making it possible for these organisms to fix CO_2 from the atmosphere. The protein

22 responsible for the organization of this lattice in beta-type carboxysomes of the

23 freshwater cyanobacterium *Synechococcus elongatus*, CcmM, occurs in two isoforms

24 thought to localize differentially within the carboxysome matrix. Here, we use widefield

25 timelapse and 3D-structured illumination microscopy (3D-SIM) to study the recruitment

26 and localization of these two isoforms. We demonstrate that this super-resolution

27   technique is capable of successfully resolving the outer protein shell of the carboxysome

28   from its internal cargo. We develop an automated analysis pipeline to analyze and

29   quantify 3D-SIM images and generate a population level description of carboxysome

30   shell protein, RuBisCO, and CcmM isoform localization. We find that both CcmM

31   isoforms colocalize in space and time, prompting a revised model of the internal

32   arrangement of the beta carboxysome.

33

34   **Introduction:**

35   RuBisCO (ribulose-1,5-bisphosphate carboxylase/oxygenase), the primary

36   enzyme of carbon fixation, is ubiquitous in autotrophic organisms. However, it is

37   notoriously inefficient and readily participates in energetically wasteful side-reactions

38   with O_2 (Andersson *et al*., 2008). Many organisms that rely on RuBisCO to acquire

39   inorganic carbon tune the enzyme's local microenvironment to achieve sufficient levels

40   of carbon fixation. While plants can do this within membrane barriers, many single-celled

41   organisms have evolved a strategy of proteinaceous compartmentalization.

42   The carboxysome is a bacterial microcompartment (BMC) found in cyanobacteria

43   and prokaryotic chemoautotrophs. Composed of thousands of individual subunits, the

44   carboxysome encapsulates RuBisCO and carbonic anhydrase (CA) within a selectively

45   permeable icosahedral shell, making survival possible at atmospheric levels of CO_2

46   (Figure 1A) (Rae *et al*., 2013; Kerfeld *et al*., 2016).

47   While evolutionarily distinct carboxysomes share many similar structural features,

48   the RuBisCO in the beta-type carboxysome (ß-carboxysome) of the freshwater

49   cyanobacterium *Synechococcus elongatus* PCC7942 is organized into a paracrystalline

50   lattice (Kaneko *et al*., 2006). The structural protein CcmM has been implicated in

51   connecting individual RuBisCO enzymes into an ordered matrix, resulting in the

52   observed dense crystalline packing (Long *et al*., 2007; Cot *et al*., 2008, Long *et al.,* 2010;

2

53   Cameron *et al*., 2013). The full-length 58kDa CcmM protein of PCC7942 is characterized

54   by an N-terminal carbonic anhydrase (CA) binding domain and three repeating domains

55   toward the C-terminal end that have sequence homology to the small subunit of

56   RuBisCO (Figure 1B) (Price *et al*., 1993). Due to an internal ribosomal entry site (IRES),

57   CcmM is translated as two isoforms, a full-length protein (M58) and a 35kDa truncated

58   version (M35) that consists of only the three small subunit like (SSU-like) domains (Long

59   *et al*., 2007; Long *et al*., 2010).

60   The current model of ß-carboxysome internal structure suggests that the small

61   subunit like domains (SSU-like) of CcmM displace some of the small subunits of the L_8S_8

62   RuBisCO holoenzyme and tether multiple enzymes together into a dense network

63   (Figure 1C) (Long *et al*., 2007; Long *et al*., 2010; Rae *et al*., 2013; Kerfeld *et al.,* 2016).

64   Co-purification and yeast 2-hybrid experiments have shown that RuBisCO readily

65   complexes with both isoforms of CcmM in PCC7942 (Long *et al*., 2007; Cot *et al*., 2008).

66   In addition, fluorescence tagging experiments have demonstrated that M35 alone is

67   capable of nucleating assembly of tagged RuBisCO if at least two of the SSU-like

68   domains are present. However, M35 is not sufficient to cause encapsulation by recruiting

69   shell components in the absence of M58 (Cameron *et al*., 2013). Densitometry analyses

70   of western blot experiments have found imbalanced ratios of RbcS to RbcL (~5:8) in

71   PCC7942 cell lysates, suggesting that the missing RbcS slots may be occupied by

72   CcmM SSU domains (Long *et al*., 2011). These findings have supported a model of

73   carboxysome architecture and step-wise assembly in which M35 nucleates a core of

74   RuBisCO. In this model, M58 is limited to a layer beneath the shell where it can interact

75   with CcmN, CA, and shell components. While this model predicts that the CcmM

76   isoforms are differentially localized and that the timing of their integration may differ,

77   these predictions have yet to be directly tested.

78   In order to test this model, we fluorescently tagged CcmM to visualize its

79   assembly and the localization of CcmM isoforms *in vivo*. Previous work has shown that

80   completely replacing CcmM with tagged fusions does not disrupt carboxysome function

81   (Long *et al.*, 2007; Cameron *et al.*, 2015). Loss of either isoform of CcmM creates

82   mutants that fail to produce carboxysomes and have a high CO_2 requirement (HCR) for

83   growth (Woodger *et al.,* 2005; Long *et al.*, 2010). However, complementation of such

84   mutants with tagged copies of CcmM has been shown to rescue this phenotype (Long *et*

85   *al*., 2007; Cameron *et al.*, 2015).

86   Here we show the successful complementation of a Δ*ccmM* mutant with a dually

87   fluorescently tagged integration of *ccmM*. This dual tagging strategy does not

88   significantly impair carboxysome formation, morphology, or function. In our timelapse

89   fluorescence microscopy data we find no evidence of differential CcmM isoform

90   assembly during carboxysome biogenesis. Using super-resolution 3D Structured

91   Illumination Microscopy (3D-SIM), we examined the relative localization of carboxysome

92   shell, CcmM, and RuBisCO proteins. Our 3D-SIM data does not support a model of

93   carboxysome internal organization in which M58 is limited to a layer just beneath the

94   external protein shell. These data support a revised model of carboxysome internal

95   structure in which M35 and M58 isoforms are both integrated deep within the core of the

96   carboxysome and are both involved with the early steps of carboxysome assembly.

97

98

99   **Results:**

100   **Fluorescent fusions to CcmM complement a deletion of the wildtype**

101

102   We integrated an N- and C-terminal fluorescently-tagged copy of *ccmM* (*mTagBFP2-*

103   *ccmM-mNeonGreen*) driven by the IPTG inducible promoter P*trc* into the genome of an

4

104   *S. elongatus* PCC7942 Δ*ccmM*::*HygR* mutant strain (Figure 2A-B) and verified

105   expression with western blot analysis (Figure 2C). This strategy allowed us to visually

106   separate full length CcmM from truncated M35 by blue fluorescence. We found that P*trc*

107   was sufficiently leaky to produce protein without induction. Consequently we never

108   induced the Δ*ccmM* + *mTagBFP2-CcmM-mNeonGreen* strain, including for western blot

109   analysis, unless otherwise noted. We blotted lysates of WT, Δ*ccmM*, and Δ*ccmM* +

110   *mTagBFP2-CcmM-mNeonGreen* strains for the presence of CcmM (Figure 2C). In WT

111   7942 cells, we detected two bands at ~60 kDa and ~40 kDa, corresponding to the two

112   native CcmM isoforms M58 and M35. In the Δ*ccmM* strain, these bands are absent. In

113   the Δ*ccmM* + *mTagBFP2-CcmM-mNeonGreen* gene complement, we detected two

114   bands at ~140 kDa and ~70 kDa, corresponding to molecular weight shifts of 60kDa

115   (both fluorescent tags) and 30kDa (mNeonGreen alone), respectively. The observed

116   weight shift of the tagged CcmM demonstrates that the CcmM IRES is not impaired by

117   the presence of N- and C-terminal tags, and that both long and short CcmM isoforms are

118   translated. We also made a reciprocally tagged version of the CcmM complement

119   (mNeonGreen-CcmM-mTagBFP2), but did not use it for further analysis because

120   western blotting showed the presence of protein degradation (Supplemental Figure S1).

121   Our tagged *ccmM* complement grew at a rate comparable to WT at atmospheric

122   levels of CO_2 (Figure 2D). We grew WT 7942, the Δ*ccmM* mutant, and the Δ*ccmM* +

123   *mTagBFP2-CcmM-mNeonGreen* complement in ambient air and 2% CO_2 conditions,

124   measured optical density at 750nm (OD_{750}), and calculated doubling times between the

125   18- and 90-hour time points. Both WT and Δ*ccmM* cells cultured with 2% CO_2 grew well

126   with similar doubling times of 17.6 ± 0.4 hours (n = 5, Error = SD) and 15.8 ± 2.1 hours

127   (n = 6, Error = SD) respectively. As expected, Δ*ccmM* mutant growth was dependent on

128   supplemented CO_2 (Long *et al.*, 2010); these cells showed no growth in ambient air

129   conditions. In contrast, the Δ*ccmM* + *mTagBFP2-CcmM-mNeonGreen* complement grew

5

130   well in air with a doubling time of 23.3 $\pm$ 2.4 hours (n = 6, Error = SD). This growth rate is

131   similar to that of WT cells in air, which had a doubling time of 20.6 $\pm$ 1.8 hours (n = 6,

132   Error = SD), indicating that our engineered strain is capable of fixing carbon, and that

133   carboxysome function is not severely impaired by the dual-fusion *ccmM* complement.

134   Because both the M58 and M35 isoforms of CcmM are required for growth without CO_2

135   supplementation (Long *et al.*, 2010), our data indicate that both isoforms produced by

136   our dual fusion are functional.

137   Carboxysomes formed in the $\Delta ccmM$ + *mTagBFP2-CcmM-mNeonGreen*

138   complement were structurally similar to those of WT cells. Using transmission electron

139   microscopy, we imaged ultrathin sections of fixed cells from WT 7942, $\Delta ccmM$, and

140     $\Delta ccmM$ + *mTagBFP2-CcmM-mNeonGreen* strains (Figure 3). Carboxysomes in WT

141   PCC7942 cells had an average maximum width of 179 $\pm$ 33 nm (n = 26, Error = SD).

142   Carboxysomes in $\Delta ccmM$ + *mTagBFP2-CcmM-mNeonGreen* cells generally had a

143   normal appearance and shape with visibly angled facets and often clear hexagonal

144   geometry, but were noticeably larger, with an average maximum diameter of 319 $\pm$ 92

145   nm (n = 41, Error = SD). This is not unexpected; it has been previously reported that His-

146   tagged *ccmM* complements increase carboxysome size (Long *et al.,* 2007).

147   Occasionally, dense masses at the cell poles were observed in $\Delta ccmM$ + *mTagBFP2-*

148   *CcmM-mNeonGreen* micrographs, most likely indicating protein aggregation. Because

149   we are using this strain without induction and no effective repressors exist, we cannot

150   know if reducing expression would prevent aggregate formation. However, IPTG-

151   induced cells observed with 3D-SIM display a dramatic increase in polar protein

152   aggregation, often filling a large portion of the cell, confirming that overexpression of this

153   construct leads to aggregation (Supplemental Figure S2).

154

155 **Both CcmM isoforms share similar recruitment kinetics and localization**

156   Both CcmM isoforms are recruited to growing carboxysomes with similar timing

157 and kinetics. Using widefield microscopy, we imaged the CcmM complement

158 (mTagBFP2-CcmM-mNeonGreen) at 10 minute intervals for 40 hours (Figure 4). Particle

159 tracking revealed that both the CcmM isoforms assembled slowly, with an average

160 assembly time of approximately 10.50 $\pm$ 5.39 hours (n = 8, Error = SD) for M58-

161 mNeonGreen and M35-mNeonGreen, and 12.06 $\pm$ 7.27 hours (n = 8, Error = SD) for

162 mTagBFP2-M58 (Figure 4C). This is longer than the ~6-7 hour maturation time

163 previously reported for RuBisCO (Chen *et al.*, 2013), perhaps as a result of temperature

164 or light levels during imaging. Assembly times were estimated based on the time it took

165 a particle to go from the intensity required for automatic particle detection (methods) to

166 the first value $\geq$ 0.8 on the normalized intensity plot.

167   Next, a four-parameter logistic equation was used to approximately model the

168 particle tracks. These models highlight similar assembly kinetics for both CcmM isoforms

169 within the same carboxysome. Based on these fit curves, half-max values of green and

170 blue particle assemblies were found to have an absolute average difference of 1.18 $\pm$

171 0.68 hours (n = 8, Error = SD). If one CcmM isoform precedes the other during

172 carboxysome biogenesis, the half-max values of each isoform would be expected to be

173 significantly different. However, a comparison of half-max values from eight measured

174 assemblies found no significant difference (Wilcoxon matched-pairs signed rank test,

175 number of pairs = 8, P = 0.945). In order to test if CcmM isoforms differ in rate of

176 assembly, channel specific assembly times (average reported above) were analyzed

177 and found not to be significantly different among paired fluorescent channels (Wilcoxon

178 matched-pairs signed rank test, number of pairs = 8, P = 0.375). This indicates that

179 CcmM isoforms M35 and M58 assembled at relatively similar rates.

180

7

181 **M58 is not confined to a sub-shell layer in the carboxysome**

182 Super-resolution microscopy of fluorescently tagged M58 and M35 show

183 indistinguishable distributions in the carboxysome. We used 3D-Structured Illumination

184 Microscopy (3D-SIM) to acquire super-resolution images of the Δ*ccmM* + *mTagBFP2-*

185 *CcmM-mNeonGreen* strain, as well as fluorescently tagged RuBisCO (RbcL-sfGFP) and

186 the shell protein CcmK4 (CcmK4-mTagBFP2 and CcmK4-sfGFP) in PCC7942. 3D-SIM

187 images of strains with both GFP- and BFP-tagged CcmK4 resolved the external

188 carboxysome shell as a ring structure in the xy-plane (Figure 5A-F), demonstrating that

189 3D-SIM provides sufficient resolution to identify peripherally localized proteins in the

190 carboxysome. To confirm these rings were not an artifact of SIM reconstruction, we

191 imaged a strain of PCC7942 integrated with a GFP labeled copy of the large subunit of

192 RuBisCO (RbcL-sfGFP). This strain has been previously used successfully to study

193 RuBisCO assembly and spacing (Savage *et al*., 2010; Chen *et al*., 2013). 3D-SIM of

194 RbcL-sfGFP showed no ring-like structures, producing only solid regularly-spaced

195 particles (Figure 5G-I). To test if M58 was in fact limited to a sub-shell layer, we imaged

196 the Δ*ccmM* + *mTagBFP2-CcmM-mNeonGreen* gene complement with 3D-SIM. Both

197 CcmM isoforms produced solid objects similar to those observed with the RbcL-sfGFP

198 strain (Figure 5J-N). These qualitative results suggested that the tagged M58 isoform of

199 CcmM was not excluded from integration into the carboxysome core as would be

200 expected if the protein was only present as a thin layer just beneath the exterior shell.

201 The reconstructed intensity histogram (RIH) score from the SIMcheck plugin (Ball *et al*.,

202 2015) was used to verify reconstruction quality. Reconstruction scores for all conditions

203 were of similar quality (Supplemental Table S1).

204 We developed an automated image analysis pipeline and a metric to quantify the

205 degree to which fluorescently-labeled proteins were localized at the perimeter of the

206 carboxysome versus uniformly distributed throughout the matrix. The max-to-center

8

207   intensity (MTC) ratio is calculated for each particle as the peak intensity of the average

208   radial profile divided by the intensity at the particle centroid. A perfectly uniform protein

209   distribution would result in the peak particle intensity overlapping the particle centroid,

210   and yield an MTC ratio of 1.00. Higher MTC values result from particles with decreased

211   intensity at their centers, indicating a more ring-link appearance.

212   ANOVA testing confirmed that mean MTC values were significantly

213   heterogeneous between all the labeled carboxysome proteins (Welch's ANOVA, $F_{4,}$

214    $_{7378}$=160.48, P<0.001). A Games-Howell test with $q_{critical}$(k=5, df=∞, α=0.001)=5.484 was

215   then used to make further pairwise comparisons of labeled carboxysome protein MTC

216   values (Supplementary Table S2). This automated analysis of RbcL-sfGFP and CcmK4-

217   sfGFP images confirmed our initial observations that carboxysomes appear

218   fundamentally different between these strains (Games-Howell test, MD=0.02, q=22.26);

219   similar results were obtained from the comparison of RbcL-sfGFP and CcmK4-

220   mTagBFP2 (Games-Howell test, MD=0.03, q=26.38) (Figure 6A). RbcL-sfGFP particles

221   had an average diameter of 244 $\pm$ 45 nm and an average MTC value of 1.002 $\pm$ 0.005 (n

222   = 3505), with a maximum intensity ratio of 1.04. Based on this, we calculated an upper

223   ratio threshold of 1.05, below which objects are likely to be uniform, by adding two

224   standard deviations to the RbcL-sfGFP max ratio of 1.04. This threshold is denoted on

225   MTC ratio versus diameter plots as a horizontal dotted line (Figure 6).

226   In contrast to RbcL, we found that shell proteins displayed high MTC ratios.

227   CcmK4-sfGFP particles had an average diameter of 253 $\pm$ 34 nm (n = 3459), and in

228   comparison to RbcL-sfGFP particles, a significantly greater average MTC ratio of 1.023

229    $\pm$ 0.077 (Games-Howell test, MD=0.02, q=22.26) (Figure 6H). Approximately 10% of

230   CcmK4-sfGFP particles have MTC ratios $\geq$ 1.05, denoting a ring-like appearance (Figure

231   6B). Analysis of CcmK4-mTagBFP2 particles also revealed a significantly different mean

232   MTC ratio compared to labeled RbcL-sfGFP (Games-Howell test, MD=0.03, q=26.38)

9

233   (Figure 6H), with the CcmK4-mTagBFP2 particles having an average size of 244 $\pm$ 32

234   nm and average MTC ratio of 1.036 $\pm$ 0.093 (Figure 6C). Of note, the percent of ring-like

235   particles identified in CcmK4-mTagBFP2 cells (18.16% $\geq$ $MTC_{1.05}$) was significantly

236   greater than the percentage found in CcmK4-sfGFP cells (9.90% $\geq$ $MTC_{1.05}$) (Games-

237   Howell test, MD=0.01, q=8.51) (Figure 6H). This increase in the fraction of rings

238   identified with BFP labeled CcmK4 over those identified with GFP may be the result of

239   the improvement in resolution due to the shorter wavelength of blue versus green

240   fluorophores. Based on the smallest resolvable shell in the CcmK4-mTagBFP2 strain,

241   which had an apparent diameter of 197nm, and accounting for an expected shell depth

242   of 5-6nm, we do not expect to resolve by SIM even true ring-like particles smaller than

243   approximately 220nm in diameter (Kaneko *et al.*, 2006). This lower resolvable limit is

244   denoted on plots of tagged M58 and of M35 particles by a grey region in Figure 6D-E.

245   Analysis of the $\Delta ccmM$ + *mTagBFP2-CcmM-mNeonGreen* gene complement

246   identified a small number of tagged M58 particles as ring-like (Figure 6D). Our analysis

247   found 0.58% (19 of 3303) of the mTagBFP2-M58 particles had MTC ratios of $\geq$ 1.05,

248   with an average size of 233 $\pm$ 46 nm and average MTC ratio of 1.003 $\pm$ 0.010 (Figure

249   6F). We found a significant difference in the MTC ratios of mTagBFP2-M58 particles vs

250   both shell-labeled CcmK4-mTagBFP2 (Games-Howell test, MD=0.03, q=25.27) and

251   CcmK4-sfGFP (Games-Howell test, MD=0.02, q=20.69) (Figure 6H). This supports

252   qualitative observations that particles of the labeled M58 strain did not appear as ring-

253   like as those in the strains with labeled carboxysome shells. mTagBFP2-M58 particles

254   also had significantly different MTC ratios compared to RbcL-sfGFP particles (Games-

255   Howell test, MD=0.001, q=10.05), but this difference was produced by only 19 ring-like

256   particles in the mTagBFP2-M58 strain (Figure 6H). Taken together, these test results

257   indicate that though mTagBFP2-M58 labeled carboxysomes have a small but statistically

258   significant number of MTC ratios $\geq$ 1.05, the mean ratio is not similar to that produced by

10

259   labeled carboxysome shell proteins, as would have been expected if the M58 isoform

260   followed a strict sub-shell localization.

261   The Δ*ccmM + mTagBFP2-CcmM-mNeonGreen* complement, which expresses

262   both full-length M58-mNeonGreen and the short isoform M35-mNeonGreen, produced 2

263   particles with MTC ratios ≥ 1.05 (Figure 6E). Only 0.06% of particles were found above

264   that threshold, with an average size of 244 ± 47 nm (*n* = 3437) and average MTC ratio of

265   1.002 ± 0.005 (Figure 6F). The mean MTC ratio of these particles was significantly

266   different than those of both labeled CcmK4-sfGFP (Games-Howell test, MD=0.02,

267   *q*=22.20) and CcmK4-mTagBFP2 (Games-Howell test, MD=0.03, *q*=26.34) (Figure 6H).

268   Pair-wise comparison of M58-mNeonGreen and M35-mNeonGreen particles to RbcL-

269   sfGFP found no significant difference in mean MTC ratios (Games-Howell test,

270   MD=0.00005, *q*=0.57) (Figure 6G), indicating that the population of green fluorescent

271   particles produced in the Δ*ccmM* + mTagBFP2-CcmM-mNeonGreen strain were solid,

272   similar to those observed in the strain with labeled RuBisCO.

273

274   **Discussion:**

275   **The carboxysome can support the addition of large foreign proteins via direct**

276   **fusion to CcmM**

277   The function of CcmM and other components of the carboxysome are robust to

278   the addition of large protein fusions, further supporting these fusions as a means to

279   localize foreign cargo to the carboxysome for engineering applications. Previous work

280   has shown that tagged CcmM gene complements can rescue the HCR phenotype of

281   CcmM mutants without significant impairment of carboxysome function compared to WT

282   cells (Long *et al.*, 2010; Cameron *et al.*, 2015). We find that such complementation is

283   also possible when fluorescent tags are fused to both ends of CcmM, significantly

284   increasing the size of both the M58 and M35 isoforms. These results suggest that

11

285   heterologous proteins could be simultaneously fused to multiple loci in the matrix,

286   opening the door for localizing multipart enzymatic pathways inside the carboxysome.

287

288   **M35 and M58 assemble simultaneously during carboxysome biogenesis**

289   M35 has been hypothesized to coordinate the organized paracrystalline cargo

290   assembly of RuBisCO, with M58 limited to a peripheral sub-shell layer (Long *et al.,* 2007;

291   Cot *et al.,* 2008; Long *et al*., 2010; Long *et al*., 2011; Rae *et al*., 2013). Based on this

292   architecture, we expected M35 to assemble prior to M58 in the same manner as shell

293   recruitment follows RuBisCO (Chen *et al*., 2013). However, we were unable to resolve

294   any significant temporal difference between the CcmM isoforms. This concurrent timing

295   suggests that M58 interacts with RuBisCO even at the early stages of carboxysome

296   assembly, possibly in the internal core of the carboxysome. Assuming that the

297   carboxysome core grows by addition of material to the outside of a stable paracrystalline

298   RuBisCO assembly (Chen *et al*., 2013), these results also suggest that M58 does not

299   assemble as a separate layer around a pre-existing M35/RuBisCO core.

300

301   **M58 is not exclusive to a subshell layer**

302   3D-SIM experiments and quantitative analysis do not support a model of

303   carboxysome internal structure in which M58 is limited to a sub-shell localization. The

304   preexisting model described above proposes that M58 is not present within the primary

305   M35-Rubisco matrix. This makes logical sense based on the fact that M35, which does

306   not contain the N-terminal domain, presumably can achieve denser packing of RuBisCO

307   enzymes.

308   We expected that if M58 was in fact limited to a sub-shell layer ~5-6nm beneath

309   the outer surface, it would appear as a ring similar to CcmK4 by 3D-SIM. While SIM

310   imaging of CcmK4 did reveal the expected ring-like distribution, carboxysomes with

12

311   fluorescently-labeled M58 appeared predominantly as solid objects, with only a very a

312   small population (0.58%) showing dips in fluorescence intensity at their centers.

313   Consequently, we find no strong evidence by super-resolution microscopy to support a

314   model of carboxysome structure in which M58 is excluded from the carboxysome core,

315   suggesting that the internal carboxysome structure contains a mixed population of both

316   M35 and M58 coordinating with RuBisCO.

317   This finding raises new questions about the biogenesis of carboxysomes. For

318   example, M58 is thought to play a role in recruitment of shell components (Cot *et al.*,

319   2008; Long *et al.,* 2011; Kinney *et al.*, 2012; Cameron *et al.*, 2013). However, shell

320   proteins are recruited to carboxysomes only late in their maturation process (Chen *et al.,*

321   2013). Therefore, if M58 is present even at the early stages of carboxysome assembly,

322   what factors are responsible for delaying shell recruitment? This question is a promising

323   avenue for future work.

324

325   **Materials and Methods:**

326   **Western blot analysis**

327   For SDS-PAGE, log-phase (OD_{750} = 1.0) cultures of cyanobacterial strains were

328   pelleted and frozen at -20°C. Frozen pellets were thawed in B-PER Bacterial Protein

329   Extraction Reagent (ThermoScientific), without DNAse or Lysozyme, and normalized by

330   wet pellet mass. Resuspended cells were mixed directly with SDS loading buffer and

331   boiled. Boiled samples were run on a 4-20% Tris-Glycine NuPAGE gel (Invitrogen) at

332   120V. SDS-PAGE separated proteins were transferred to a nitrocellulose membrane

333   with an iBlot2 transfer device (ThermoScientific).

334   The membrane was blocked with 5% skim milk in TBST (50mM Tris, 150mM

335   NaCl, 0.1% Tween 20), then probed with 1:10,000 of anti-CcmM primary antibody (a gift

336   of Ben Long), followed by a horseradish peroxidase-conjugated goat anti-rabbit

13

337   secondary antibody (Agrisera AS09 602). The membrane was incubated with

338   SuperSignal West Dura Extended Duration chemiluminescent substrate

339   (Thermoscientific) and imaged with the Bio-Rad ChemiDoc system.

340

341   **Transmission Electron Microscopy**

342   For TEM experiments, 1mL of mid-log cultures were pelleted (6k rpm, 5 min) and

343   concentrated 2x in sterile dH_2O. The cells were then mixed 1:1 with fixative (1.25%

344   formaldehyde, 2.5% glutaraldehyde, 0.03% picric acid, 0.1M sodium cacodylate buffer,

345   pH 7.4), incubated at RT for 30 min, then pelleted and stored in fixative at 4°C overnight.

346   Fixed cells were embedded in epon resin and cut into ultra-thin sections (~60-80nm).

347   Sections were stained with uranyl acetate and lead citrate, then imaged on a Tecnai G2

348   Spirit Bio TWIN TEM.

349

350   **Cell culture**

351   Wild-type, mutant, and modified strains of *Synechococcus elongatus* PCC7942

352   were grown in BG-11 media, with 1 g/L HEPES adjusted to pH 8.5. Cultures were grown

353   at 30-35°C under constant light with an approximate intensity of 1000 lm/m^2. Cultures

354   were grown in 125ml or 250ml flat bottom flasks, shaking at 150 rpm. Wild type 7942

355   and knockout complements were grown with ambient air conditions. Mutant

356    $\Delta ccmM$::*HygR* cultures were supplemented with 2% CO_2 and 25 µg/mL hygromycin B.

357   Strains with fluorescently labeled carboxysome components, carrying kanamycin or

358   spectinomycin resistance genes, were grown with 25 µg/mL kanamycin or 25µg/mL

359   spectinomycin respectively. For the CcmM complement strain, $\Delta ccmM$ + *mTagBFP2-*

360   *CcmM-mNeonGreen*, cultures were grown with 5 µg/mL kanamycin and 25 µg/mL

361   hygromycin B. For growth curve experiments, biological replicates were made by

362   isolating colonies grown on BG11 agar with 1 g/L HEPES, 50mM HCO_3^-, and 1mM

14

363   $Na_2S_2O_3$. Isolates were screened by PCR to confirm the presence or absence of the WT

364   *ccmM* gene. Growth curve cultures were prepared by washing starter cultures in fresh

365   BG11 pH 8.5 media, then diluting to OD750 of ~0.1 in 40 mL BG11 in 250mL flat bottom

366   flasks.

367

368   **Image acquisition**

369   For both conventional fluorescence and 3D-SIM experiments, 5μL of either mid-

370   log cells (OD_{750} = 1-2) for timelapse experiments or early-log cells (OD_{750} = 0.5 - 1.2) for

371   3D-SIM were spotted on 2% agarose BG11 pads. Agarose pads were placed sample-

372   side down in MatTek 35mm glass bottom microwell dishes with No. 1.5 coverslips.

373   Sterile water was spotted within the dish to mitigate dehydration of the agarose pad, and

374   the dish was sealed with parafilm. Though strains expressing labeled CcmM were under

375   the control of the IPTG inducible promoter P*trc*, no induction was used with these cells

376   due to adequate basal expression. Cells expressing RbcL-sfGFP were imaged on BG11

377   agarose pads with the addition of 50μM IPTG following previously reported protocols

378   (Savage *et al.*, 2010). SIM of uninduced RbcL-sfGFP cells also produced solid particles,

379   but were not as bright as induced cells and produced several false-positives in our

380   analysis pipeline (Supplemental figure S3). For timelapse experiments, samples were

381   recovered for >1h at 34-35°C, under ~1000 lm/m^2, and in ambient air, before being

382   imaged using a Nikon TE2000 and a 100x oil objective. Cells were kept at 30°C under

383   ~800 lm/m^2 light intensity during timelapse, and imaged every 10min.

384   3D-SIM data was collected on a DeltaVision OMX V4 Blaze system (GE

385   Healthcare) equipped with a 60x / 1.42 N.A. Plan Apo oil immersion objective lens

386   (Olympus), and three Edge 5.5 sCMOS cameras (PCO). mTagBFP2 fluorescence was

387   excited with a 405nm laser and collected with a 477/35 emission filter, mNeonGreen with

388   a 514nm laser and 541/22 emission filter, and sfGFP with a 488nm laser and a 528/48

15

389   emission filter. Z-stacks of ~2 microns were acquired with a z-step of 125 nm and with

390   15 raw images per plane (five phases, three angles). Spherical aberration was

391   minimized using immersion oil matching (Hiraoka *et al.*, 1990). Super-resolution images

392   were computationally reconstructed from the raw datasets with a channel-specific

393   measured optical transfer function (OTF) and a Wiener filter constant of 0.001 using

394   CUDA-accelerated 3D-SIM reconstruction code based on Gustafsson *et al.*

395   *(*2008). Axial chromatic aberration was measured using TetraSpeck beads (Thermo

396   Fisher) a nano-grid control slide and multi-channel datasets were registered using the

397   image registration function in softWoRx.

398

399   **Image analysis**

400   SIM datasets were imported into MATLAB (Mathworks) using the bioformats

401   reader, followed by thresholding and background subtraction. The threshold value was

402   empirically determined and assessed by visualizing the resultant centroid position and

403   mask in MATLAB and Imaris (Bitplane AG) respectively. Segmented objects were further

404   analyzed if they met a cutoff for volume, surface area, sphericity, major-minor axis ratio,

405   and mean radius.

406   We calculated the MTC (max to center) ratio for each object. From the centroid,

407   the radially averaged intensity for each sub-sampled (0.5 pixels) radius was measured.

408   This was done for each Z-plane and then averaged over the Z-axis. A polynomial curve

409   was fit to the averaged radial profile of each segmented object in MATLAB. The most

410   suitable polynomial fit (up to 6th order) was selected based on meeting the Bayesian

411   Information Criterion. Then, the 1st and 2nd derivative of each fitted curve were

412   calculated to find the root with the global maximum. The intensity at this root was

413   calculated and divided by the intensity at the centroid. This ratio was calculated for each

414   object and plotted versus its mean radius in MATLAB.

16

415   Notably, the resolvable carboxysome ring limit of 220nm that we estimate in our

416   analysis is well above the ~110nm theoretical resolution limit of 3D-SIM (at 520nm

417   wavelength; Gustafsson *et al.,* 2000; Gustafsson *et al*., 2008). The difference is likely

418   due to a combination of practical limitations along with the probable overestimation of

419   carboxysome diameter in our analysis pipeline due to convolution of the true object size

420   with the point spread function in the fluorescence images.

421   Timelapse data of Δ*ccmM* + *mTagBFP2-CcmM-mNeonGreen* were processed

422   with ImageJ (FIJI) (Schindelin *et al*., 2012). Timelapse data from two sequential

423   acquisitions of the same field of view were imported into FIJI with the Bio-Formats Import

424   plugin with autoscaling, concatenated, and separated by channel. Channels were

425   registered using rigid registration in the StackReg FIJI plugin, then background

426   subtracted with a 50-pixel radius rolling ball. Particle tracking was performed in FIJI with

427   the TrackMate plugin using the LoG detector (Laplacian of Gaussian filter) with 0.5μm

428   estimated blob diameter, 0.5 threshold, and sub-pixel localization. Automatically

429   generated tracks were manually extended backwards in time 20-30 frames by selecting

430   0.5μm diameter regions at or near site where the particle was first detected in order to

431   capture a background fluorescence level. Particle tracks were corrected for

432   photobleaching by dividing intensities by an average of 7 reference particles, normalized

433   to the first frame of the time lapse, in each channel. Reference particles were objects

434   observed to be relatively stable compared to particles that lost or gained fluorescence

435   due to carboxysome biogenesis. The same reference particles were used for correction

436   in both channels. To generate the timelapse montage, brightness and contrast values

437   were manually adjusted separately in each channel to enhance visibility in the figure.

438

439   **Cloning and strain construction**

440   Plasmids used for *S. elongatus* strain construction were made by Gibson

441   assembly. Tagged CcmM plasmids were cloned by inserting the *ccmM* gene, along with

442   mNeonGreen and mTagBFP2 coding sequences with additional flexible linker

443   sequences, into the previously described pDFS21 neutral site II (NS2) integration

444   plasmid downstream of the IPTG inducible P*trc* promoter (Savage *et al*., 2010). The

445   *ccmM* gene was obtained directly from the *S. elongatus* PCC7942 genome via PCR with

446   Phusion polymerase (NEB). The *ccmK4* gene for cloning shell fusion plasmids was

447   obtained as a synthesized gBlock (IDT) and cloned into the pDFS21 integration plasmid.

448   *S. elongatus* strains were transformed with integration plasmids by incubating ~5

449   fold concentrated OD_{750} 1-2 culture with 10-100ng plasmid at $30^{o}C$ in the dark overnight,

450   followed by plating transformants on selective BG11 agar (Clerico *et al*., 2007). The

451   mutant Δ*ccmM* strain was made by integrating a hygromycin B resistance gene into the

452   native *ccmM* ORF, followed by selective plating and screening (Sachdeva G., 2014).

453

454   **Acknowledgements**

464

465   **References**

18

466   Andersson I, Backlund A. (2008). Structure and function of Rubisco. Plant Physio
467   and Biochem. 46:275-291.
468
469   Badger MR, Hanson D, Price GD. (2002). Evolution and diversity of CO2
470   concentrating mechanisms in cyanobacteria. Funct. Plant Biol. 29:161–
471   173.
472
473   Badger MR, Price GD. (2003). CO2 concentrating mechanisms in cyanobacteria:
474   molecular components, their diversity and evolution. J Exp.
475   Bot. 54:609–622.
476
477   Ball G, Demmerle J, Kaufmann R, Davis I, Dobbie IM, Schermelleh L. (2015).
478   SIMcheck: a Toolbox for Successful Super-resolution Structured Illumination
479   Microscopy. Sci Rep. 5:15915.
480
481   Berla BM, Saha R, Immethun CM, Maranas CD, Moon TS, Pakrasi HB. (2013).
482   Synthetic biology of cyanobacteria: unique challenges and opportunities. Front
483   Microbiol. 4(246):1-14.
484
485   Cameron JC, Wilson SC, Bernstein SL, Kerfeld CA. (2013). Biogenesis of a
486   bacterial organelle: the carboxysome assembly pathway. Cell. 155:1131-1140.
487
488   Chen AH, Robinson-Mosher A, Savage DF, Silver PA. Polka JK. (2013). The
489   bacterial carbon-fixing organelle is formed by shell envelopment of preassembled
490   cargo. PLOS One. 8(9):1-13.
491
492   Clerico EM, Ditty JL, Golden SS. (2007). Specialized techniques for site-directed
493   mutagenesis in cyanobacteria. Methods Mol Biol. 362:155-171.
494
495   Cot SS, So AK, Espie GS. (2008). A multiprotein bicarbonate dehydration
496   complex essential to carboxysome function in cyanobacteria. J Bacteriol.
497   190:936-945.
498
499   Gustafsson MGL. (2000). Surpassing the lateral resolution limit by a factor of two
500   using structured illumination microscopy. J of Microsc. 198(2):82-87.
501
502   Gustafsson MGL, Shao L, Carlton PM, Wang CJR, Golubovskaya IN, Cande WZ,
503   Agard DA, Sedat JW. (2008). Three-dimensional resolution doubling in wide-field
504   fluorescence microscopy by structured illumination. Biophys J. 94:4957-4970.
505
506   Hiraoka Y, Sedat JW, Agard DA. (1990). Determination of three-dimensional
507   imaging properties of a light microscope system. Partial confocal behavior in
508   epifluorescence microscopy. Biophys J. 57(2):325-333.
509

510 Kaneko Y, Danev R, Nagayama K, Nakamoto H. (2006). Intact carboxysomes in
511 cyanobacterial cell visualized by Hilbert Differential Contrast Transmission
512 Electron Microscopy. J Bacteriol. 188(2):805-808.
513
514
515 Kerfeld CA, Melnicki MR. (2016). Assembly, function and evolution of
516 cyanobacterial carboxysomes. 32:66-75.
517
518 Kinney JN, Salmeen A, Cai F, Kerfeld CA. (2012). Elucidating essential role of
519 conserved carboxysomal protein CcmN reveals common feature of bacterial
520 microcompartment assembly. 2012. J Biol Chem. 287(21):17729-17736.
521
522 Long BM, Murray BR, Whitney SM, Price GD. (2007). Analysis of carboxysomes
523 from *Synechococcus* PCC7942 reveals multiple rubisco Complexes with
524 carboxysomal proteins CcmM and CcaA. J Biol Chem. 282(40):29323-29335.
525
526 Long BM, Rae BD, Badger MR, Price GD. (2011). Over-expression of the ß-
527 carboxysomal CcmM protein in *Synechococcus* PCC7942 reveals a tight co-
528 regulation of carboxysomal carbonic anhydrase (CcaA) and M58 content.
529 Photosynth Res. 109:33-45.
530
531 Long BM, Tucker L, Badger MR, Price GD. (2010). Functional cyanobacterial ß-
532 carboxysomes have an absolute requirement for both long and short forms of the
533 CcmM Protein. Plant Physiol. 153:285-293.
534
535 Polka JK, Silver PA. (2013). Building synthetic cellular organization. Mol Biol Cell.
536 24:3585-3587
537
538 Price GD, Howitt SM, Harrison K, Badger MR. (1993). Analysis of a genomic
539 DNA region from the cyanobacterium *Synechococcus* sp. Strain PCC7942
540 involved in carboxysome assembly and function. J Bacteriol. 175(10):2871-2879.
541
542 Price GD, Badger MR, Woodger FJ, Long BM. (2007). Advances in
543 understanding the cyanobacterial CO_2-concentrating-mechanism (CCM):
544 functional components, Ci transporters, diversity, genetic regulation and
545 prospects for engineering into plants. J Exper Bot. 59(7):1441-1461.
546
547 Rae BD, Long BM, Badger MR, Price GD. (2012). Structural determinants of the
548 outershell of ß-carboxysomes in *Synechococcus elongatus* PCC7942: roles for
549 CcmK2, K3-K4, CcmO, and CcmL. PLOS One. 7(8):1-11.
550
551 Rae BD, Long BM, Badger MR, Price GD. (2013). Functions, compositions, and
552 evolutions of the two types of carboxysomes: polyhedral microcompartments that
553 facilitate CO_2 fixation in cyanobacteria and some proteobacteria. Microbiol Mol
554 Biol Rev. 77(3):357-379.
555

556   Rae BD, Long BM, Whitehead LF, Förster B, Badger MR, Price GD. (2013).
557   Cyanobacterial carboxysomes: microcompartments that facilitate CO_2 fixation. J
558   Mol Microbiol Biotechnol. 23:300-307.
559
560   Sachdeva G. (2014). Controlling fluxes for microbial metabolic engineering.
561   Doctoral dissertation, Harvard University.
562
563   Savage DF, Afonso B, Chen AH, Silver PA. (2010). Spatially ordered dynamics
564   of the bacterial carbon fixation machinery. Science. 327:1258-1261.
565
566   Schindelin J, Arganda-Carreras I, Frise E. *et al*. (2012). Fiji: an open-source
567   platform for biological-image analysis. Nature Methods. 9(7): 676-682.
568
569   Schindelin J, Rueden CT, Hiner MC, Eliceiri KW. (2015). The ImageJ ecosystem:
570   An open platform for biomedical image analysis. Mol Reprod Dev. 82(7-8):518-
571   29.
572
573   Tanaka S, Sawaya M, Philips M, Yeates T. (2008). Insights from multiple
574   structures of the shell proteins from the ß-carboxysome. Prot Sci. 18:108-120.
575
576   Woodger FJ, Badger MR, Price GD. (2005). Sensing of inorganic carbon
577   limitation in *Synechococcus* PCC7942 is correlated with the size of the internal
578   inorganic carbon pool and involves oxygen. Plant Physiol. 139(4):1959-1969.
579
580   Yokoo R, Hood RD, Savage DF. (2015). Live-cell imaging of cyanobacteria.
581   Photosynth Res. 126(1):33-46.
582
583
584
585
586
587
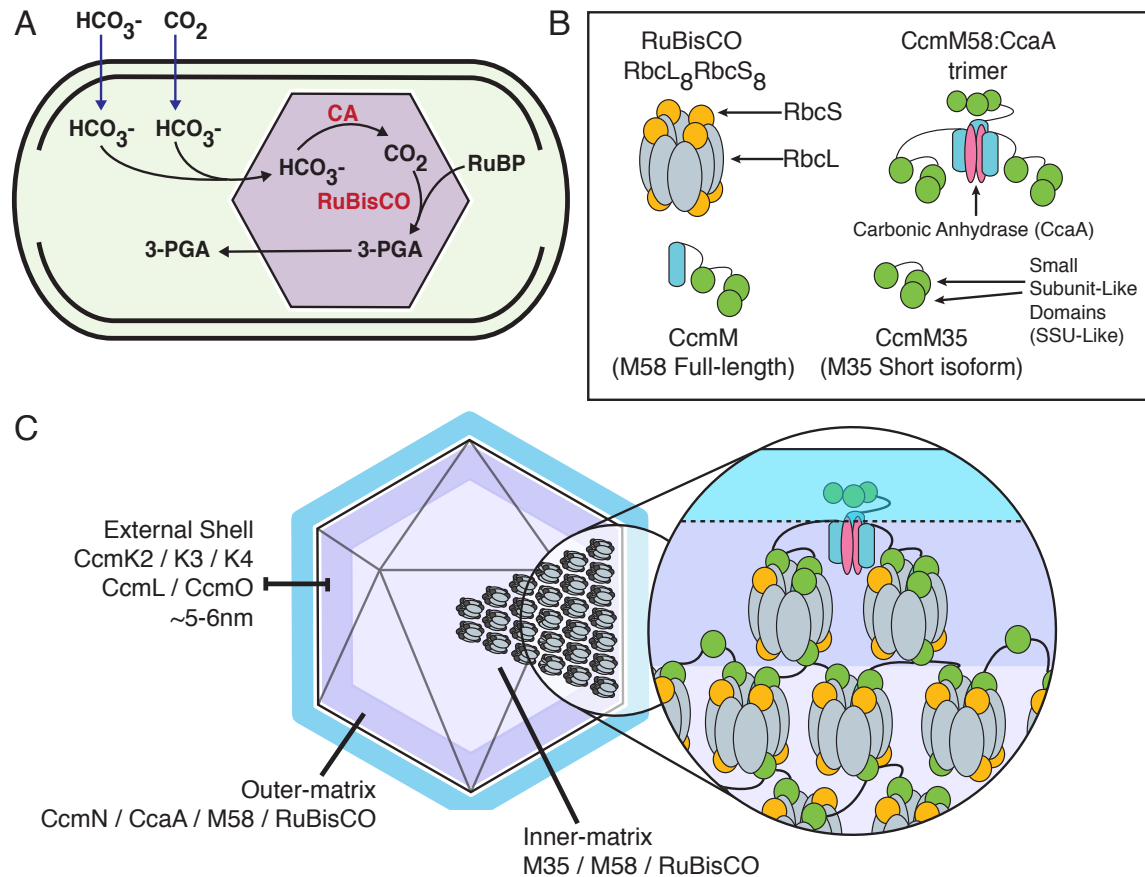588
589
590
591
592
593
594
595

596
597 Figure 1. Current model of the cyanobacterial carboxysome internal structure.
598 (A) *S. elongatus* utilizes the carboxysome to concentrate and protect its
599 RuBisCO enzymes. Through a multi-step process, bicarbonate passes into the
600 carboxysome, is converted to CO_2 by carbonic anhydrase, and is then fixed by
601 RuBisCO to form 3-phosphoglyceric acid (3-PGA). (B) Legend of proteins and
602 protein complexes of the carboxysomes interior. *CcmM* is an essential
603 carboxysome gene that is translated as two different isoforms, the full-length
604 58kDa M58 and a truncated 35kDa form, M35. CcmM has an N-terminal domain
605 that complexes with CcaA carbonic anhydrase, and three repetitive C-terminal
606 domains that have homology with the small subunit of RuBisCO. (C) These small
607 subunit-like domains (SSU-like), which make up the majority of the M35 protein,
608 are believed to displace a portion of the RuBisCO small subunits and physically
609 tether the enzymes together within the core of the carboxysome, to the exclusion
610 of the long M58 isoform which has been hypothesized to remain just beneath the
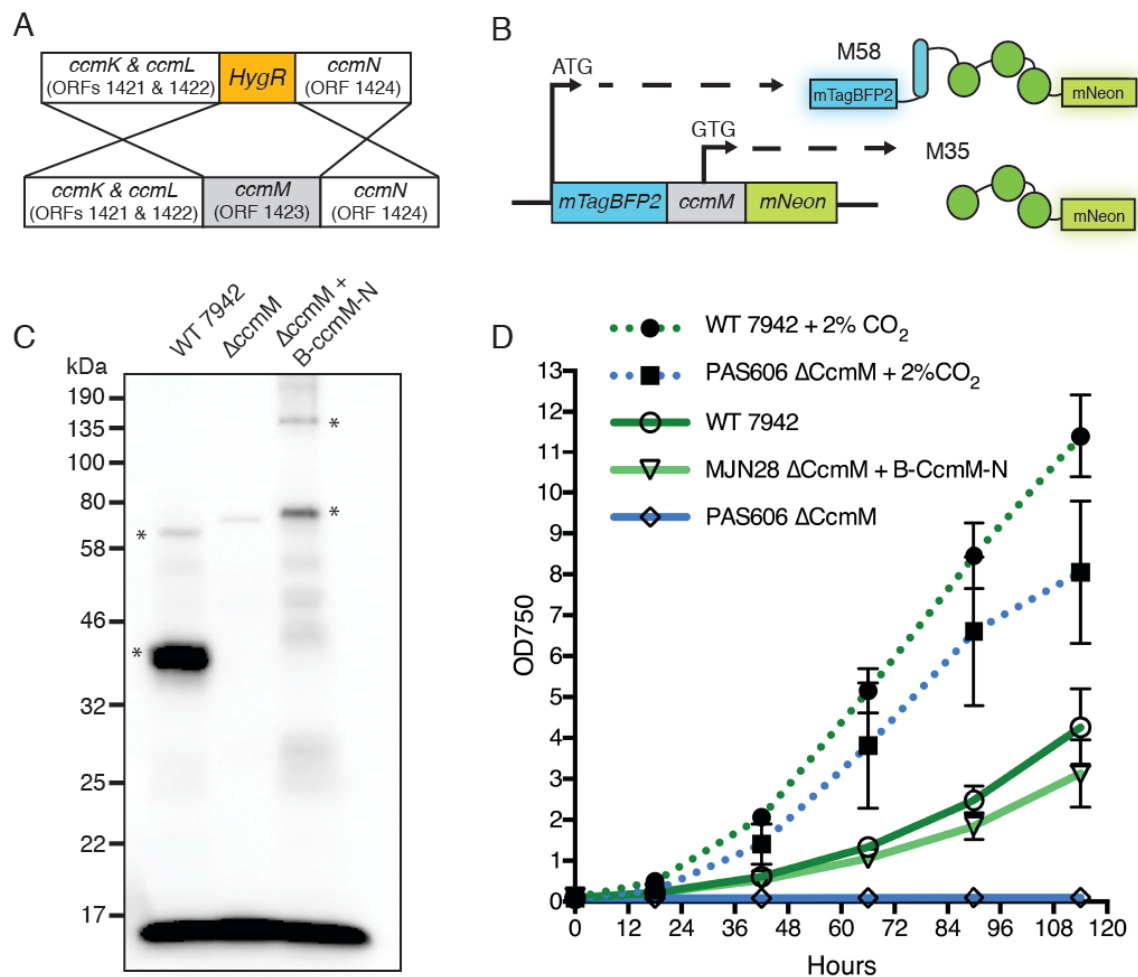611 carboxysome shell.

22

612
613 Figure 2. Fluorescently tagged *ccmM* integrated into the genome of a Δ*ccmM*
614 knockout produces both CcmM isoforms and and restores growth in ambient air
615 conditions. (A) The Δ*ccmM* knockout was made by integrating a hygromycin
616 resistance marker into the genomic site of *ccmM*. (B) Diagram of fluorescently
617 tagged *ccmM*. N- and C-terminal fusions of mTagBFP2 and mNeonGreen
618 produces short and long isoforms with different fluorescent characteristics. This
619 construct was integrated at Neutral Site II of the 7942 Δ*ccmM* genome to yield
620 the Δ*ccmM* + *mTagBFP2-CcmM-mNeonGreen (+B-ccmM-N)* strain. (C) Anti-
621 CcmM western blot of WT, Δ*ccmM*, and *+B-ccmM-N*. Full length M58 isoform of
622 CcmM is ~58 kDa, while the truncated M35 is ~35 kDa. The fluorescent fusions
623 of mTagBFP2-M58-mNeonGreen and M35-mNeonGreen have expected
624 molecular weights of approximately 113 kDa and 63 kDa respectively. (D)
625 Growth curves of WT 7942, Δ*ccmM*, and the *+B-ccmM-N* genetic complement.
626 Dotted lines denote cultures grown with 2% supplemented CO_2. Solid lines
627 denote cultures grown in ambient air conditions. n = 3 biological replicates, error
628 bars = standard deviation.

23

A   *S. elongatus* PCC7942

B   *S. elongatus ΔccmM::HygB*

C   *S. elongatus ΔccmM::HygB + mTagBFP2-ccmM-mNeonGreen*

629
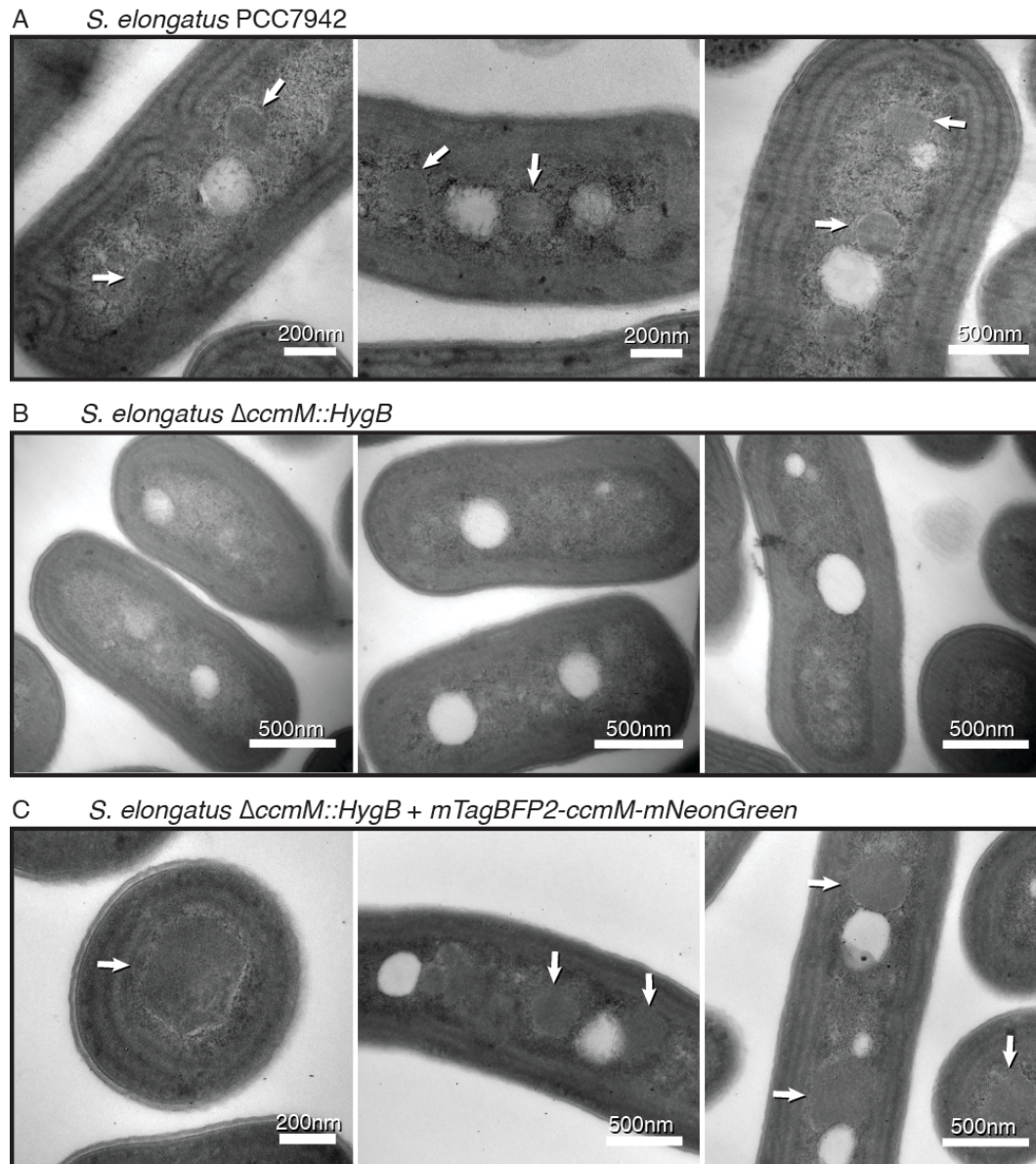630 Figure 3. Transmission electron micrographs show the formation of
631 carboxysomes in Δ*ccmM* cells complemented with fluorescently tagged *ccmM*.
632 (A-D) Carboxysomes (white arrows) in wild type PCC7942 cells show
633 characteristic hexagonal geometry. Diameters of WT carboxysomes labeled in
634 micrographs range from 150 - 280 nm with an average of 180 $\pm$ 33nm (N=???).
635 (E-H) Micrographs of the Δ*ccmM* knockout show the absence of carboxysomes.
636 (I-L) Integration of the fluorescently tagged *ccmM* construct *B-ccmM-N* into the
637 Δ*ccmM* knock out rescues the formation of apparently normal carboxysomes.
638 These carboxysomes had geometry similar to that observed in wild type cells.
639 Carboxysomes with tagged CcmM appeared to range more widely in size than in
640 wild type cells with an average diameter of 319 $\pm$ 92nm (N=???). Some (J & L)
641 were of typical size (200nm in diameter), while others (K) are larger at 300-330
642 nm. Larger carboxysomes were also observed, like that seen in (I), which
643 approaches 600nm at its widest point.

24

644
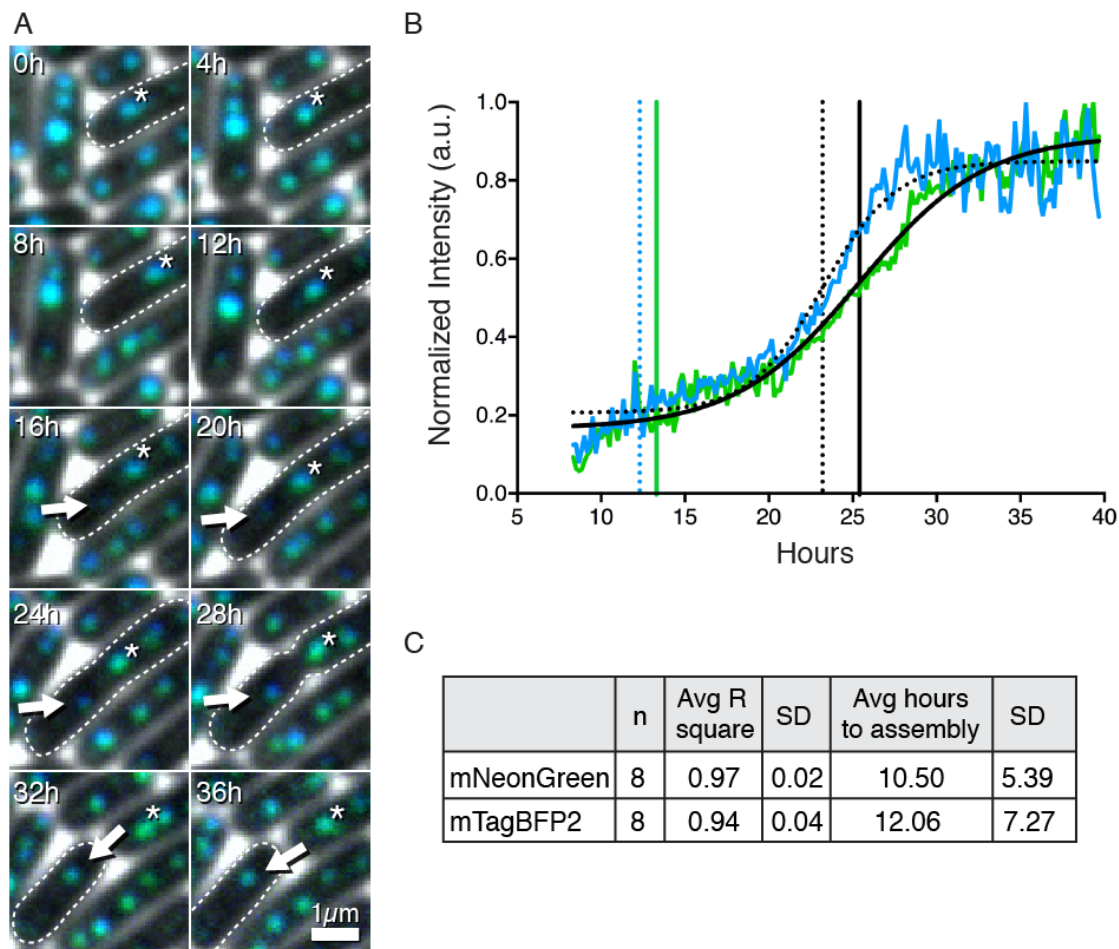
645
646 Figure 4. CcmM isoforms co-assemble at the site of new carboxysomes. (A)
647 Merged montage of carboxysome biogenesis in the Δ*ccmM* + *mTagBFP2-ccmM-*
648 *mNeonGreen* gene complement strain shows simultaneous co-localization of
649 both blue (mTagBFP2-M58) and green (M58-mNeonGreen / M35-mNeonGreen)
650 particles. White arrows indicate the new carboxysome. White asterisk indicates
651 the parent carboxysome. (B) Channel specific intensity plots of carboxysome
652 biogenesis depicted in panel A reveal sigmoidal-like dynamics in assembly timing
653 in M35 and M58 CcmM isoforms. Vertical blue and green lines denote point at
654 which automatic particle tracking first identified the new carboxysome. Tracks
655 were extended backwards to measure background by manually measuring spot
656 at or near the new particle (Methods). Four-parameter logistic equations were fit
657 to each track; black solid or dotted vertical lines denote half-max values of each
658 channel. (C) Statistics of sigmoidal curves fit to 8 measured biogenesis events
659 find similar assembly dynamics in both green and blue channels. Assembly time
660 was measured from first time point of automatic tracking to first value ≥ 0.8 on
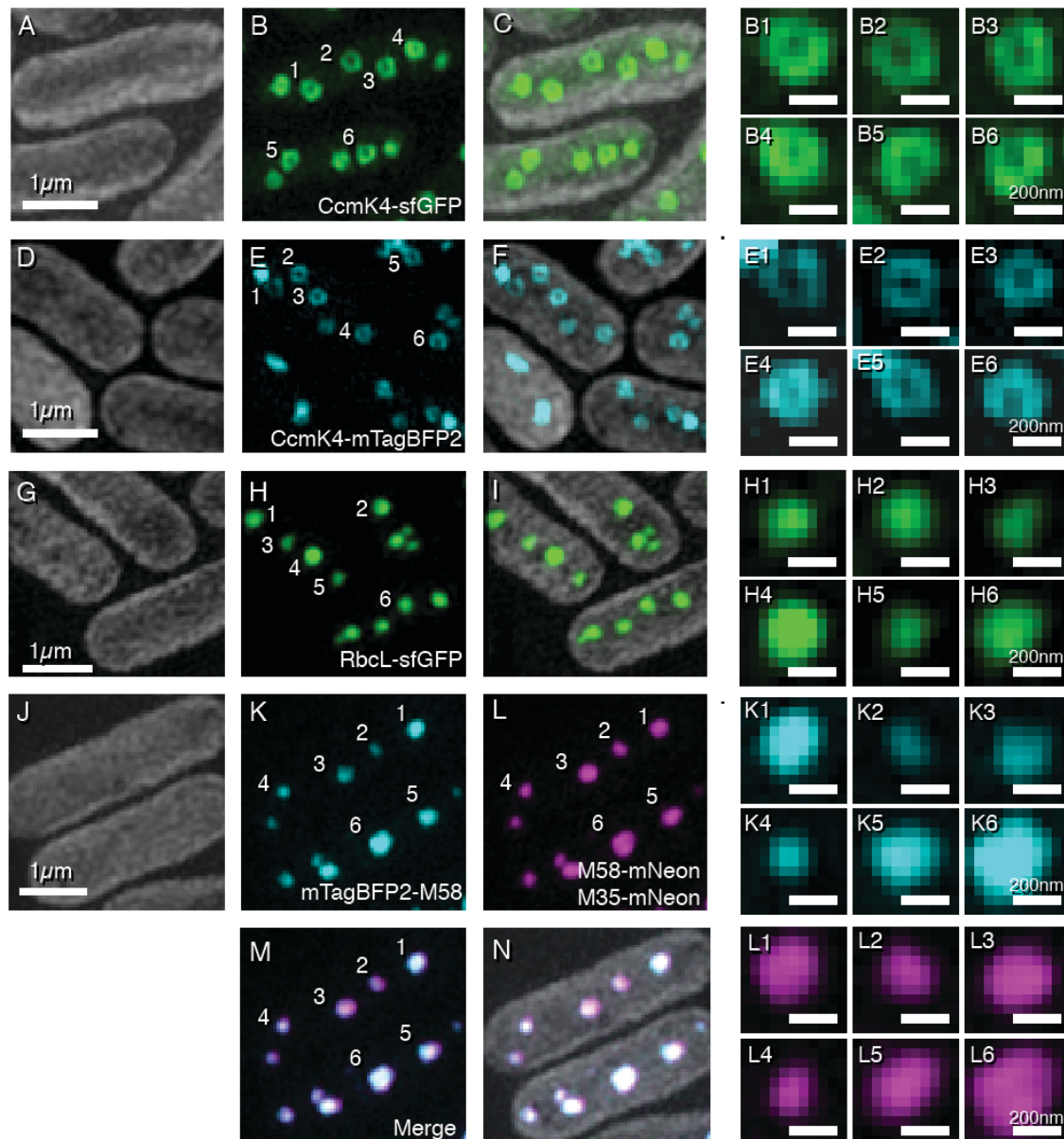661 normalized intensity plot.
662

25

Figure 5. SIM of fluorescently tagged carboxysomes resolves the ring of the outer shell, and an absence of shell-like localization of either RuBisCO or CcmM. (A-C) SIM of CcmK4-mTagBFP2 resolves the carboxysome shell as a hollow ring, while (D-F) SIM of RbcL-sfGFP produces solid particles. (G-K) SIM of *ΔccmM + mTagBFP2-ccmM-mNeonGreen* produces RuBisCO-like, apparently solid particles. M35/M58-mNeonGreen particles are pseudocolored magenta. Numbers identify individual carboxysomes and correspond to magnified panels on the right.

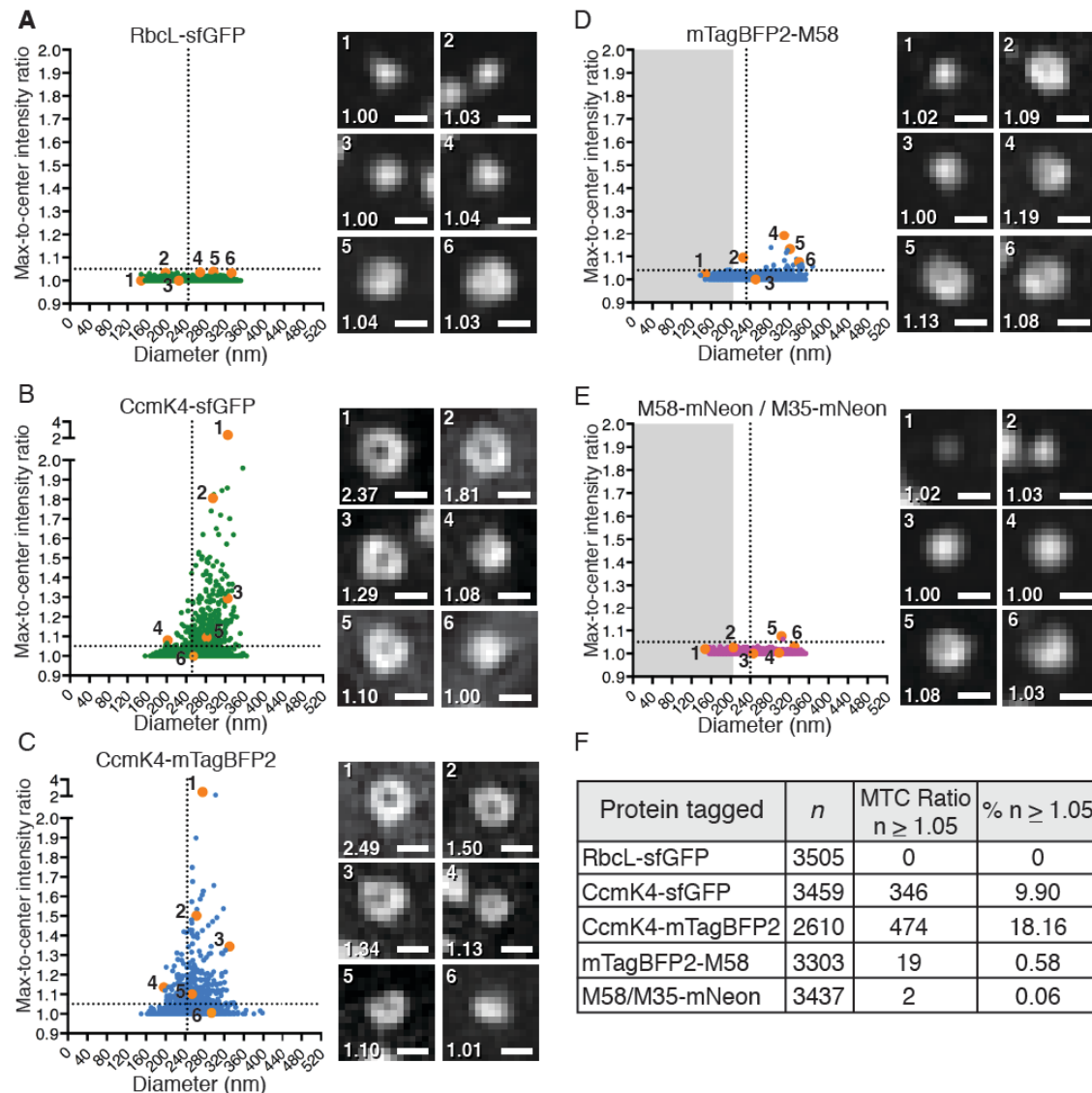| Protein tagged	n	MTC Ratio n ≥ 1.05	% n ≥ 1.05
RbcL-sfGFP	3505	0	0
CcmK4-sfGFP	3459	346	9.90
CcmK4-mTagBFP2	2610	474	18.16
mTagBFP2-M58	3303	19	0.58
M58/M35-mNeon	3437	2	0.06

Figure 6. Analysis of 3D-SIM data. Using radially averaged intensity profiles of fluorescent particles in 3D-SIM data, maximum intensity to center (MTC) intensity ratios can measure the degree to which a fluorescent object is resolved as a ring. (A) Analysis of RbcL-sfGFP 3D-SIM data found no objects with a max-to-center ratio (MTC) greater than 1.04, with an average ratio of 1.002 $\pm$ 0.005 and average particle size of 244 $\pm$ 45 nm marked by the vertical line. An upper ratio limit of 1.05, below which objects are likely to be solid, was calculated by adding two standard deviations to the RbcL-sfGFP max ratio. The 1.05 MTC cutoff is marked by a horizontal line on all plots. (B) Size versus intensity ratio plot of CcmK4-sfGFP shows a population of particles (345, 9.97%) with MTC ratios $\geq$ 1.05. (C) Plot of CcmK4-mTagBFP2 shows a two-fold increase in the fraction of ring-like particles compared to the GFP tagged version (474, 18.16%). (D) Analysis of particles in the blue channel of the $\Delta ccmM \pm mTagBFP2\text{-}CcmM\text{-}mNeonGreen$ strain, representing M58, finds only a few particles with noticeable ring-like appearance (19, 0.58%), with the vast majority of particles appearing

27

688 solid. Based on the size of smallest detected ring in the tagged shell strains
689 (196nm) and a shell thickness of 5-6nm, the minimum diameter at which ring-like
690 shapes can be detected is calculated as 220nm; this is marked in gray. Ring-like
691 particles within this region are unlikely to be resolved due to their small size. (E)
692 Plot of particles in the green channel of Δ*ccmM* ± *mTagBFP2-CcmM-*
693 *mNeonGreen* strain, representing M58-mNeonGreen and M35-mNeonGreen are
694 predominantly solid with only 2 ring-like structures identified (2, 0.06%). (F) Table
695 summarizing analysis statistics. In microscopy panels, scale bars are 200nm,
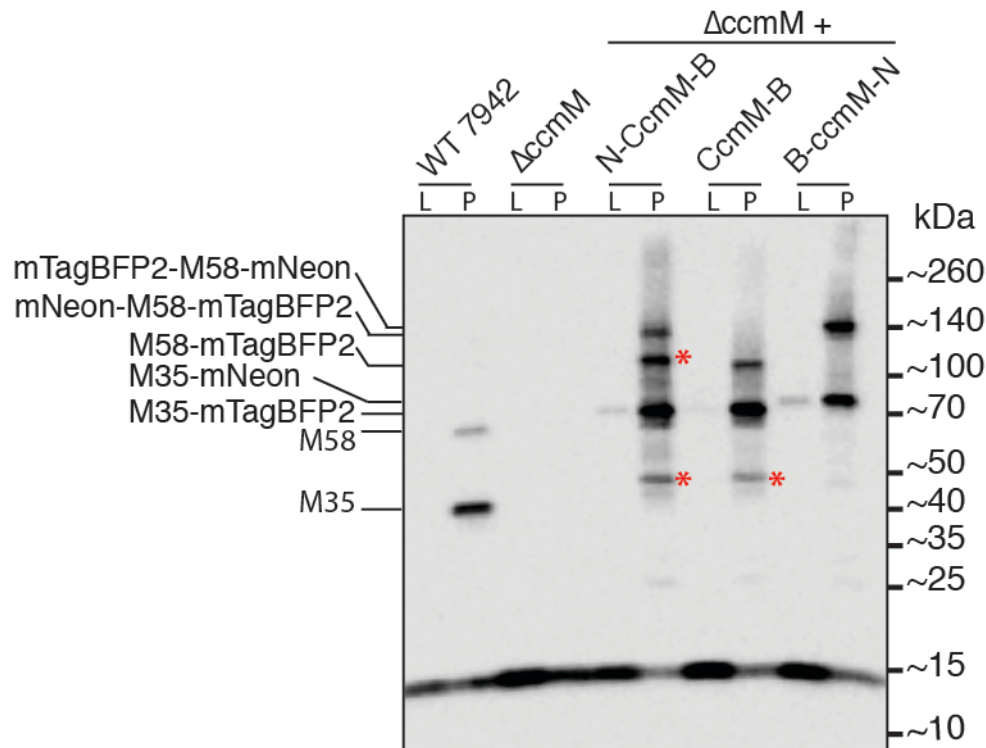696 and numbers denote MTC ratio.
697
698
699
700
701
702
703
704
705
706
707
708
709
710
711
712
713
714
715
716
717
718
719
720
721
722
723
724
725

726
727 Figure S1. Protein degradation in variant *ccmM* gene complements. Western blot
728 analysis of Δ*ccmM + mNeonGreen-ccmM-mTagBFP2*, and Δ*ccmM + ccmM-mTagBFP2*
729 revealed prominent unexpected bands (marked by red asterix) that could be indicative of
730 protein degradation in the cell. The Δ*ccmM + mTagBFP2-ccmM-mNeonGreen* strain did
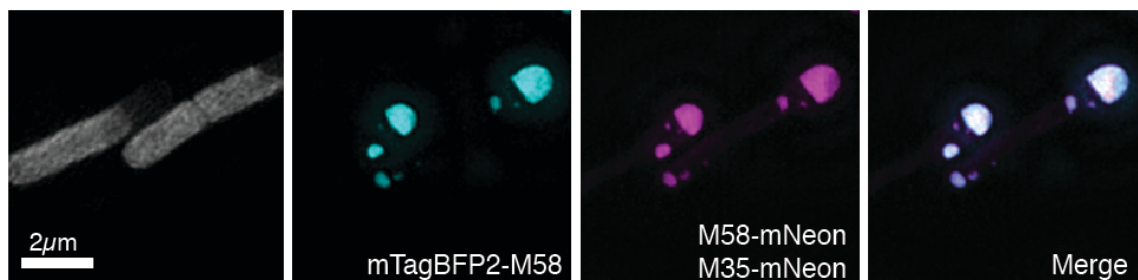731 not show similar unexpected bands. L = cell lysate and P = post-lysis pellet.
732

733
734 Figure S2. Induction of the P*trc*::Δ*ccmM + mTagBFP2-ccmM-mNeonGreen* in *S.*
735 *elongatus* leads to protein aggregation. SIM images of Δ*ccmM + mTagBFP2-ccmM-*
736 *mNeonGreen* cells induced with 50µM IPTG show large aggregations of fluorescent
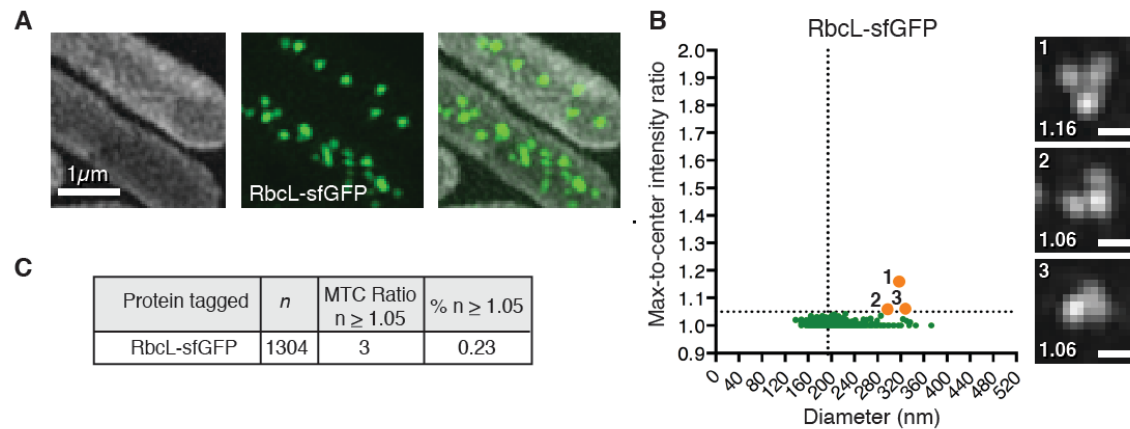737 signal near the cell polls.

738
739 Figure S3. Uninduced cells expressing RbcL-sfGFP still produce solid particles.
740 Qualitative data and image analysis results of PCC7942 RbcL-sfGFP cells without any
741 IPTG induction show similar incidence of low MTC ratio solid particles compared to cells
742 induced with 50μM IPTG. Three particles were identified as ring-like with MTC ratios >
743 1.05, but were confirmed to be three particle clusters incorrectly analyzed as single
744 objects by our analysis program.
745
746

Strain	Tag	IPTG (μM)	# Imgs	Refractive Index	Wiener Filter	RIH (477)	RIH (528)	RIH (541)	RIH (608)
DFS724	RbcL-sfGFP	50	31	1.518	0.01		12.74 ± 1.63		2.78 ± 0.66
AHC134	CcmK4-sfGFP	-	31	1.517	0.01		13.15 ± 1.78		3.53 ± 1.08
MJN31	CcmK4-mTagBFP2	0	29	1.517	0.01	8.28 ± 1.84			2.77 ± 0.96
MJN28	mTagBFP2-CcmM-mNeon	0	47	1.517	0.01	9.45 ± 2.80		12.58 ± 2.51	3.10 ± 0.84

747
748 Tables S1. Structured Illumination Microscopy reconstruction scores. Reconstructed
749 Intensity Histogram scores (RIH) were averaged across all image sets for each strain
750 used for image analysis. Scores of 6-12 are considered good, and greater than 12
751 excellent. Columns with RIH scores are channel specific. Channel 608 captured the red
752 auto-fluorescence of cells which was not used for any analysis. Error = Standard
753 deviation.
754

A

Welch's ANOVA	Degrees of freedom	F_s	P
Among groups	4.00	160.48	6.51 x 10-132
Within groups	7377.44		

B

Games-Howell test	Mean difference	q	> q_{crit} 5.484 (α=0.001)
CcmM-mNeon vs CcmK4-sfGFP	0.020465	22.20	Significant
CcmM-mNeon vs CcmK4-mTagBFP2	0.033914	26.34	Significant
CcmM-mNeon vs mTagBFP2-CcmM	0.001283	9.56	Significant
CcmM-mNeon vs RbcL-sfGFP	0.000050	0.57	Not significant
CcmK4-sfGFP vs CcmK4-mTagBFP2	0.013449	8.51	Significant
CcmK4-sfGFP vs mTagBFP2-CcmM	0.019182	20.69	Significant
CcmK4-sfGFP vs RbcL-sfGFP	0.020515	22.26	Significant
CcmK4-mTagBFP2 vs mTagBFP2-CcmM	0.032631	25.27	Significant
CcmK4-mTagBFP2 vs RbcL-sfGFP	0.033964	26.38	Significant
mTagBFP2-CcmM vs RbcL-sfGFP	0.001333	10.05	Significant

755
756 Table S2. Statistical test results of particle MTC ratio comparison.
757
758

Strain or Plasmid	Genotype	Resistance	Reference
E-coli strains			
DH5-alpha	Host strain for plasmid construction (PAS644)		
DH10-beta	Host strain for plasmid construction (PAS641, PAS642, PAS643)		
Turbo	Host strain for plasmid construction (PAS645)		
S. elongatus strains			
PCC7942	Wild-type *Synechococcus elongatus,* ATCC 33912		
Δ*ccmM*	PCC7942 Δ*ccmM*::*HygR* knock out	HygB	
PAS646	PCC7942 *Ptrc:CcmK4-mNeon* integrated in NS2	Kan	This work
PAS647	PCC7942 Δ*CcmM::HygR* + *Ptrc:mNeon-CcmM-mTagBFP2* integrated in NS2	HygB, Kan	This work
PAS648	PCC7942 Δ*CcmM::HygR* + *Ptrc:CcmM-mTagBFP2* integrated in NS2	HygB, Kan	This work
PAS649	PCC7942 Δ*CcmM::HygR* + *Ptrc:mTagBFP2-CcmM-mNeon* integrated in NS2	HygB, Kan	This work
PAS650	PCC7942 *Ptrc:CcmK4-mTagBFP2* integrated in NS2	Kan	This work
PAS651	PCC7942 *Papca:CcmK4-mNeon* integrated in NS1	Sp	Chen et al., 2013
PAS652	PCC7942 *Ptrc:RbcL-sfGFP* integrated in NS2	Kan	Savage et al., 2010
Plasmids			
pAM2314	*S. elongatus* Neutral Site I integration vector	Sp	Mackey et al., 2007
pAM1579	*S. elongatus* Neutral Site II integration vector	Kan	Mackey et al., 2007
pDFS21	derivative of pAM1579 with *trc* promoter from pTRC99 and *lacI*	Kan	Savage et al., 2010
pAHC134	P*apca*::*ccmK4-sfGFP*	Sp	Chen et al., 2013
pDFS724	P*trc*::*RbcL-sfGFP*	Kan	Savage et al., 2010
PAS641	P*trc*::*mNeonGreen-CcmM-mTagBFP2* cloned into pDFS21 at XbaI and NotI sites	Kan	This work
PAS642	P*trc*::*CcmM-mTagBFP2* cloned into pDFS21 at XbaI and NotI sites	Kan	This work
PAS643	P*trc*::*mTagBFP2-CcmM-mNeonGreen* cloned into pDFS21 at XbaI and NotI sites	Kan	This work
PAS644	*Ptrc*::*CcmK4-mNeonGreen* cloned into pDFS21 at XbaI and NotI sites	Kan	This work
PAS645	*Ptrc*::*CcmK4-mTagBFP2, mTagBFP2* cloned in place of *mNeonGreen* in pDFS21	Kan	This work

759
760 Table S3. Strains and plasmids

761
762
763